European Polymer Journal 66 (2015) 386–396

Contents lists available at ScienceDirect

European Polymer Journal

journal homepage: www.elsevier.com/locate/europolj

Macromolecular Nanotechnology

Composite films based on chitosan and nanomagnetite

Gianina A. Kloster, Norma E. Marcovich, Mirna A. Mosiewicki *

Institute of Materials Science and Technology (INTEMA), National University of Mar del Plata, Juan B. Justo 4302, 7600 Mar del Plata, Argentina

ARTICLE INFO

Article history:
Received 9 January 2015
Received in revised form 20 February 2015
Accepted 26 February 2015
Available online 5 March 2015

Keywords:
Magnetic films
Biocomposites
Chitosan
Nanomagnetite

ABSTRACT

Magnetic chitosan nanocomposite films were prepared by a simple one-step method based on the in situ co-precipitation of nanomagnetite. Both plasticized and no-plasticized films were obtained and characterized by means of X-ray diffraction (XRD), transmission electron microscopy (TEM), scanning electron microscopy (SEM), Fourier Transform infrared spectroscopy (FTIR), thermal gravimetric analysis (TGA) and mechanical (tensile) and dynamic mechanical characterization. Nanomagnetite particles formed inside chitosan films were spherical with diameters ranging from 5 to 13 nm. The film surface and morphology and mechanical behavior were greatly affected by nanoparticles concentration, leading to increasing roughness, stiffness and fragility as the iron oxide content increases. The nanoparticles interact strongly with the chitosan matrix, as was corroborated by TGA, FTIR and DRX. Even though, particles retain their magnetic characteristics and thus, composites containing more than 2 wt% NMP exhibit magnetic behavior.

1. Introduction

Magnetic nanoparticles are being extensively studied due to their interesting magnetic properties and technological applications [1,2]. In fact, small iron oxide nanoparticles have been applied in biomedical purposes for about 50 years [3,4]. This is due to their high saturation magnetization, high magnetic susceptibility, non-toxicity, chemical stability, non-carcinogenic character, biodegradability, inherent biocompatibility, ease of synthesis, relative ease to functionalize, less sensitivity to oxidation and reactive surface [4,5]. Moreover, these nanoparticles can be easily modified with biocompatible coatings as well as targeting, imaging, and therapeutic molecules [6].

Meanwhile, polymers have traditionally been considered as excellent host matrices for composite materials. Several advanced polymer nanocomposites have been synthesized with a variety of inclusions such as metals, semiconductors, carbon nanotubes and magnetic nanoparticles [1,7]. In fact, polymer matrix based nanocomposites has become a prominent area of current research and development not only due to their potential application in biotechnology but also because the incorporation of nanoparticles into polymeric matrices provides opportunities to engineer flexible nanocomposites that exhibit distinctive properties, such as magnetic, electric and antistatic. Accordingly, composite materials of polymer and magnetic nano-particles of iron oxides have attracted considerable attention of the scientific community in recent years because they often encompass the desirable features of both organic and inorganic compounds [1,8], and the very important reason for that seems to be the fact that these materials present high potential of technological applications in several fields. Magnetite nanoparticles were incorporated into polymers such as poly(vinyl alcohol), poly(ethylene glycol), poly (acrylic acid), DNA, protein and poly-saccharide matrices to improve the biocompatibility or bioactivity for biomedical application, such as magnetic cell separation, target drug delivery system and magnetic resonance imaging of clinical diagnosis [9].

Among the various polymers, the biopolymer chitosan [10], has an excellent film forming ability, high mechanical strength, biocompatibility, non-toxicity, high permeability

* Corresponding author. Tel.: +54 223 481 6600; fax: +54 223 481 0046.
E-mail address: mirna@fi.mdp.edu.ar (M.A. Mosiewicki).

http://dx.doi.org/10.1016/j.eurpolymj.2015.02.042
0014-3057/

toward water, susceptibility to chemical modifications, cost-effectiveness, etc. [9]. Chitosan is produced from N-deacetylation of chitin, a major component of crustacean shells and fungal biomass and it is readily available from seafood processing wastes [11]. This biopolymer promotes wound healing and has bacteriostatic effect and due to its positive charges at physiological pH [9], is also a bioadhesive, which increases retention at the site of application [4]. Chitosan is widely used in tissue engineering and hyperthermia region [4,12] but also, because of its high amino content, it has been found to possess good sorption capacity for many heavy metal ions through complexation with the amine groups and has been widely used as biosorbent for removing various metal ions from wastewater [11].

Many attempts have been made to improve the biocompatibility and activity of chitosan by combining it with metal oxide nanoparticles [9,13]. Due to the magnetic nature of these iron oxide–magnetite nanocomposites, they can be used for magnetically targeted cancer therapy [9,14] or may even improve the delivery and recovery of biomolecules for desired biosensing applications [9,15]. In addition, the nanoparticles have a unique ability to promote fast electron transfer between electrode and the active site of an enzyme, further improving the scope as a biosensor [9,16]. Moreover, magnetic chitosan resins have been used in biological applications such as purification of enzymes and cell separation [16]. However, most of the research efforts in this area were focused to the preparation and characterization of composite particles [11,18] while the behavior of magnetic/chitosan composite films were scarcely studied despite the good film forming properties of the biopolymer. Zhang et al. [1] indicates that magnetic nanocomposite is difficult to prepare by simple blending or mixing in solution or melt form, and thus a great deal of attentions have been placed on block copolymer-nanoparticles nanocomposites since block copolymer can self-assemble into a wide range of ordered nanostructures and nanoparticles can then be sequestered into specified domains to form ordered nanocomposites [1,17,19,20]. In spite of this, Bhatt et al. [9], dispersed magnetite nanoparticles into a chitosan solution by ultrasonication, obtaining composite films that could reach a saturated magnetization value of 10.31 emu/g with 50% doping of magnetite. In the same line, Li et al. [21] made-up chitosan/magnetite nanocomposites by in situ hybridization induced by a magnetic field, using a pre-precipitated chitosan hydrogel membrane as chemical reactor. In the present work we selected a simple one-step in situ co-precipitation method to prepare nanomagnetite–chitosan composite films. Moreover, not only the magnetic behavior of the films was proved, but also their physical, thermal and mechanical behavior was studied.

2. Experimental

2.1. Materials

Chitosan (CS) (degree of deacetylation 98%, Mv = 1.61×10^5 g/mol), supplied by PARAFARM, Mar del Plata, Argentina was used as received. Glycerol (Gly) purchased from SIGMA Aldrich was used as plasticizer. The ferric chloride ($FeCl_3 \cdot 6H_2O$), the ferric sulfate ($FeSO_4 \cdot 7H_2O$) and sodium hydroxide were obtained from Aldrich.

2.2. Methods

2.2.1. Preparation of composite films

The films were prepared by casting, some of them containing glycerol in a wt ratio glycerol/chitosan = 0.2 and 0.3. Chitosan solutions (2 wt%/v) were prepared in aqueous acetic acid (1% v/v), by magnetic stirring during 1.5 h, adding the glycerol (if applicable) in the initial mixture. A 0.2 mol/L ferric salts solution was prepared by dispersing 9 g of ferric chloride with 4.62 g of ferric sulfate (Fe^{2+}:Fe^{3+} = 1:2 M ratio) in 250 mL of aqueous acetic acid (1% v/v). An appropriate volume of the ferric salt solution (to obtain final films with 2–10 wt% nanomagnetite) was then dispersed into the chitosan solution, by magnetic stirring during 10 min. The film-forming dispersions were defoamed under rest for one hour at room temperature and then they were poured into Teflon Petri dishes (diameter = 14 cm), dried in a convective oven at 35 °C for 24 h, and kept under hood at room temperature for another day. Subsequently, the obtained films were peeled off from the plates and immersed in a NaOH aqueous solution (5 mol/L) during 0.5 h to induce the chemical co-precipitation of Fe^{2+} and Fe^{3+} ions, and then washed several times with distilled water until neutralization. Finally, the films were dried again under hood at room temperature and then kept in a closed container containing dried silica gel at room temperature (23 ± 2 °C) until testing.

2.2.2. Characterization of composite films

2.2.2.1. Thermogravimetric analysis (TGA). Thermogravimetric tests were performed in a TGA-50 Shimadzu Thermogravimetric Analyzer at a heating rate of 10 °C/min under air atmosphere (35 mL/min) from room temperature to 900 °C. Samples tested were previously dried in a vacuum oven during 2 h at 60 °C followed by 22 h at 40 °C, to remove the water moisture absorbed without degrading the film.

2.2.2.2. Infrared spectroscopy characterization. FTIR spectra of the films were recorded by the attenuated total reflection method (ATR) using a Thermo Scientific Nicolet 6700 Fourier transform infrared spectrometer. Films used in the infrared tests were about 100–150 μm thick and were previously dried in a vacuum oven at 40 °C for 48 h. The spectra were recorded over a range of 500–4000 cm^{-1} with a resolution of 2 cm^{-1} and averaged over 32 scans.

2.2.2.3. X-ray. The crystal structure of the nanocomposites was characterized by X-ray powder diffraction (XRD), using Cu Kα radiation (λ = 1.5418 Å), using a PANalytical X'Pert Pro diffractometer operated at 40 kV, 300 mA and 0.6 deg/min. Film samples were milled into powder before the tests.

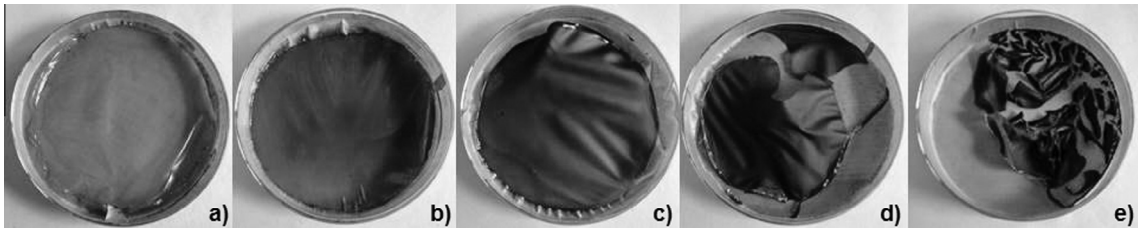

Fig. 1. Non-plasticized nanocomposite films (before inducing the chemical precipitation of the magnetic particles using NaOH). From left to right: 0 (a), 2 (b), 5 (c), 7 (d) and 10 (e) wt% nanomagnetite (nominal) concentration.

The average crystal grain sizes was calculated from the Scherrer equation with XRD line broadening assuming crystals are spherical [18],

$$\tau = \frac{0.9\lambda}{\beta \cos\theta} \quad (1)$$

where τ is the mean size of the ordered (crystalline) domains, λ is the wavelength of the X-ray (1.54056 Å), θ is the diffraction angle in degrees, and β in radians is the measured full width at half maximum intensity. The diffraction peak at $2\theta = 35.4°$, which corresponds to the lattice plane (3 1 1), was used for calculation because this peak is well resolved and shows no interferences.

2.2.2.4. Transmission electron microscopy (TEM). Transmission electron microscopy (TEM) was used to determine the morphology, size and distribution of the magnetite particles in the composite films. A JEOL 100 CX II (JAPAN, 1983) operating at 100 kV was used. The composite films were cut using a ultra-cryo-microtome and then placed onto the copper grids.

2.2.2.5. Scanning electron microscopy (SEM). The surface and the cross-section of the films (obtained by cryo-fracture after immersing samples in liquid air), were analyzed using a scanning electron microscope (JEOL, model JSM-6460 LV). For this purpose, the pieces of the films were mounted on bronze stubs using a double-sided tape and then coated with gold, before being observed under the microscope.

Table 1
Magnetite content determined from thermogravimetric measurements.

Nominal magnetite content	Glycerol content (wt%)	Mass left at 900 °C (%)	Mass of Fe_2O_3 left at 900 °C (%)	Magnetite concentration (wt%)
0	0%	4.42		
2		6.41	1.99	1.93
5		10.33	5.91	5.71
7		11.12	6.70	6.48
10		15.27	10.85	10.49
0	20%	3.15		
2		5.65	2.50	2.42
5		7.34	4.19	4.05
7		9.45	6.30	6.09
10		12.67	9.52	9.20
0	30%	1.64		
2		5.84	4.20	4.06
5		7.89	6.25	6.04
7		11.40	9.76	9.44
10		15.24	13.61	13.15

2.2.2.6. Contact angle. The surface hydrophobicity of the films was estimated by the sessile drop method, based on optical contact angle method. Contact angle measurements were carried out with a homemade instrument. A droplet of ethylene–glycol (Aldrich Co.) (5 μL) was deposited on the film surface with an automatic piston syringe. The drop image was photographed using a digital camera after 3.5 min of the drop deposition. An image analyzer was used to measure the angle formed between the surface of the film in contact with the drop, and the tangent to the drop of liquid at the point of contact with the film surface. All the samples were conditioned at 65% RH for three days before the test. Three parallel measurements were performed for each side of the films at 24 ± 2 °C.

2.2.2.7. Moisture sorption. The films, dried at 40 °C for three days in a vacuum oven, were placed inside an environmental chamber maintained at 95% relative humidity (RH) and 23 ± 2 °C, to obtain water sorption kinetics. Samples were taken out of the chamber at regular time intervals and weighed with a precision of ±0.0001 g. The equilibrium moisture content (EMC) of the films was calculated relating the weight of the samples when reached equilibrium (W_∞) with its initial (dry) weight (W_0), as follows:

$$\mathrm{EMC} = \frac{W_\infty - W_0}{W_0} * 100 \quad (2)$$

To ensure the reproducibility of the results, four specimens of each sample were tested. The absorption curves of the films were fitted according to Fick's diffusion equation for the unidimensional diffusion of a solute into a sheet [22]:

$$\frac{M_t}{M_\infty} = 1 - \frac{8}{\pi^2}\sum_{n=0}^{\infty}\frac{1}{(2n+1)^2}\exp\left[-D\frac{(2n+1)^2\pi^2 t}{1^2}\right] \quad (3)$$

where M_∞ is the amount of water absorbed at equilibrium, D is the effective diffusion coefficient, t is the time, M_t is the amount of water absorbed at time t and l is the average thickness of the film. To ensure the reproducibility of the results, four specimens for each sample were tested.

2.2.2.8. Tensile properties. Tensile tests were performed at room temperature (23 ± 2 °C) using an Instron Universal Testing Machine model 8501. The specimens were cut into strips of 5 × 25 mm. Five specimens from each film were

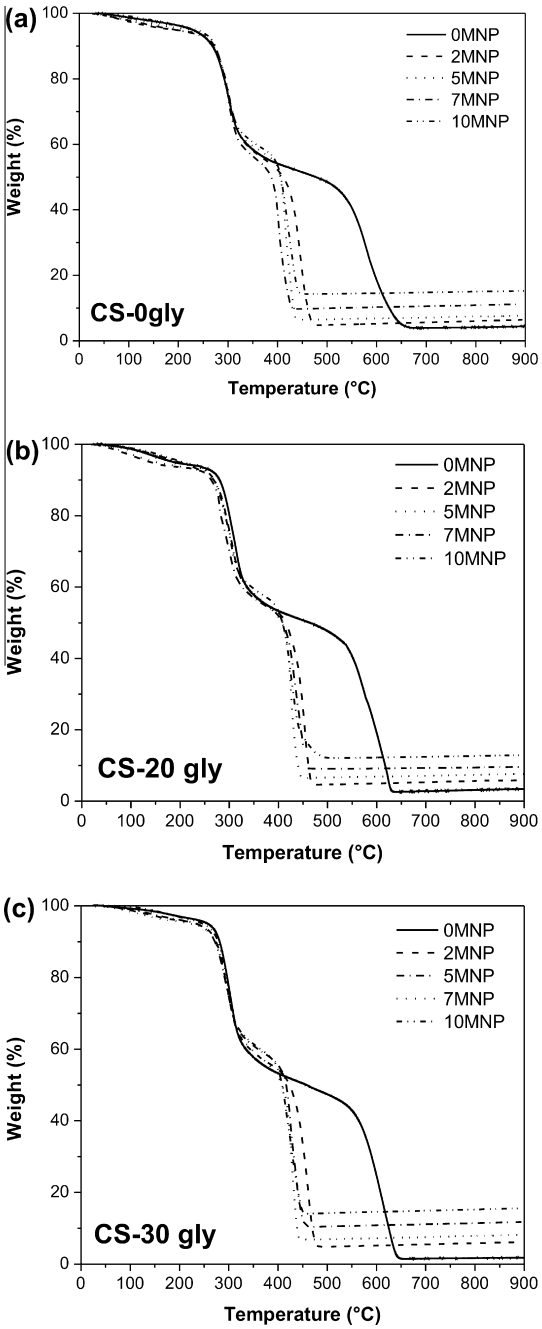

Fig. 2. TGA curves of nanomagnetite composite films: (a) non-plasticized; (b) containing 20 wt% glycerol; and (c) containing 30 wt% glycerol.

tested from a minimum of three films per sample. Crosshead speed was set at 10 mm/min. The ultimate strength (σ_b), elongation at break (ε_b) and elastic modulus (E) were calculated as described in ASTM D638-94b (ASTM, 1994). Prior to running mechanical tests, films were conditioned for 72 h at 65 ± 5% RH at room temperature.

2.2.2.9. Thermomechanical characterization. Dynamical mechanical analysis was carried out in a Perkin Elmer DMA 7 equipment. An uniaxial static stress of 800 kPa was superimposed to an oscillating uniaxial mechanical stress of 450 kPa and impressed on filmstrips at 1 Hz. Temperature scans (from 15 to 220 °C) were performed at a heating rate of 10 °C/min. The set up was used to determine the storage modulus E', the loss modulus E'' and the ratio of these two parameters, $\tan\delta = E''/E'$. Films were conditioned for 72 h at 65 ± 5% RH at room temperature prior testing.

3. Results and discussion

Fig. 1 presents the images of the non-plasticized nanocomposite films obtained with different contents of iron salts, before inducing the chemical precipitation of the magnetic particles using NaOH. It is clear that the fragility of the films increases as the iron salts concentration increases, leading to totally brittle materials that break easily and cannot be manipulated without cracking for concentrations of 7 wt% and higher. This behavior was also observed for the films plasticized with 20 and 30 wt% glycerol, although the particle concentration threshold increased, leading to quite flexible films until 7 and 10 wt% magnetite, respectively.

The final iron oxide particle concentration of the composite films was determined from thermogravimetric measurements. From the residual mass left at 900 °C, the inorganic particle content was calculated considering that the residual char corresponds to chitosan (or chitosan + glycerol) and ferric oxide (Fe_2O_3). The residual mass corresponding to the matrix was subtracted from the residual char of the composite samples and then, the difference was converted to magnetite mass. The results obtained are presented in Table 1. It is clear that the actual concentration of nanomagnetite differs from the nominal ones with no clear trend, neither respect to the magnetite concentration nor the glycerol addition, sometimes underestimating but other overestimating the real values.

The complete TGA curves, shown in Fig. 2, also provide other interesting information: from Fig. 2a, which shows the thermal degradation curves of the composites prepared without glycerol, it is noticed that all samples loose mass

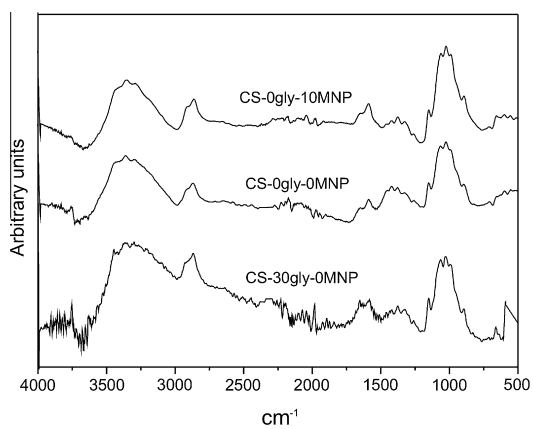

Fig. 3. FTIR spectra of the films.

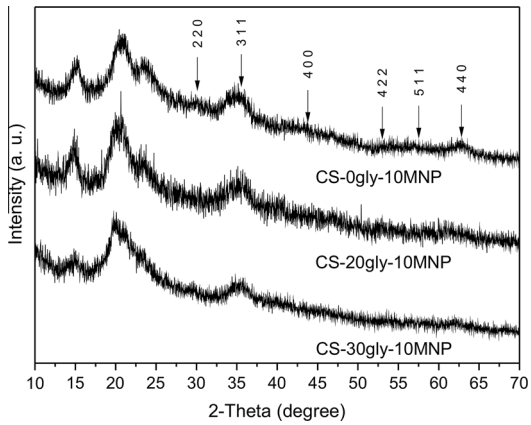

Fig. 4. XRD patterns of selected magnetic chitosan films (10 wt% MNP) with and without glycerol.

at low rate until reaching 250 °C, with weight loss of about 7 wt%, which might be due to the loss of the residual impurities [11] plus structure water not eliminated during the pre-conditioning of the samples (drying step in vacuum at low temperature). The second (~32%) at 250–310 °C and the third (starting from 310 °C) weight loss steps are considered to arise from decomposition of the chitosan matrix [23]. However, it should be noticed that the behavior of the composites during this last step of thermal degradation differs completely from the response of the neat chitosan film: the composites lost most of their mass in a narrow range of temperature (between 310 and 400 °C) while the matrix exhibits another change in the degradation rate at about 520 °C to finally converts in residual char at about 660 °C. These differences indicate clearly that there were strong interactions developed between the magnetic nanoparticles, which, in this case, reduced the thermal stability of the matrix. In this respect, Belessi et al. [24] and Hritcu et al. [25] indicated that the reduction in the thermal stability of the matrix could be attributed to the fact that the chitosan deposited on the surface of the magnetic particles in the framework of the hybrid structure has lower crystallinity compared to the free chitosan with a well-developed polymeric structure. A highly crystalline material has a more rigid molecular structure and thus, more energy should be applied to achieve its thermal degradation [26].

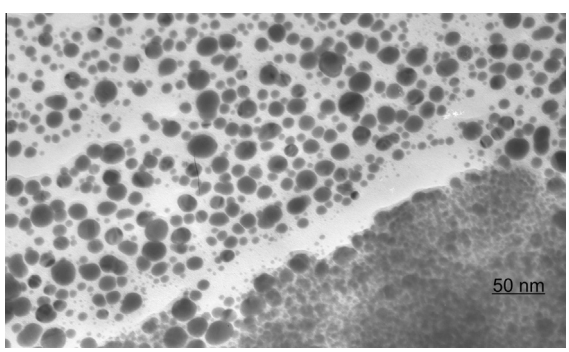

Fig. 5. TEM micrography of the unplasticized film with 10 wt% of MNP.

Fig. 2b and c, which correspond to glycerol-plasticized composites, present essentially the same behavior than Fig. 2a, confirming essentially that there is not loss of free glycerol and that the interactions developed between the plasticized matrix and the inorganic particles are similar to those developed between nanomagnetite and neat chitosan.

The FTIR spectra of films are shown in Fig. 3. The spectrum of the neat chitosan film (CS-0gly-0MNP) shows a broad band centered on 3250 cm^{-1} assigned to —OH hydrogen bonded with contribution of the $—NH_2$ group-stretching vibration [27,28]. No evidence of free OH bond stretch (3600 cm^{-1}) appears in this spectrum. The peaks at 2920 and 2876 cm^{-1} correspond to CH_2 and CH (tertiary), respectively [23]. The two bands appearing at 1630 and 1515 cm^{-1} are characteristic to the ammonium side chains [29]. They can be assigned to the $\delta_{as}NH^+$ and δ_sNH^+ bending modes, respectively. The characteristic band at 1730 cm^{-1} observed in chitosan films obtained at low pH is lacking (C═O stretching, at low pH the amide is protonated, which breaks up the conjugated system of the amide group resulting in a "normal" C═O group), indicating that the amide is not protonated in the neat film. The band centered at 1375 cm^{-1} as well the shoulder observed at 1333 cm^{-1} are assigned to the vibrations of CH_3 in amide group and CH/CH_2 stretching vibrations in the pyranose ring, respectively [27]. In the wavenumber range of C—C and C—O stretching, the typical bands at 1090, 1065 and 1120 cm^{-1} are observed [29]. The small peak at 900 cm^{-1} corresponds to the β linkage of the glucoside rings [23]. There are, however, several differences between the spectra of the neat and magnetite-containing samples. In the spectra of the magnetic samples, the relative intensities of the bands at 3000–3600 cm^{-1}, which can be related to concentration of amino groups of chitosan and those assigned to the ammonium side chain (1630 and 1515 cm^{-1}) decreased [29,30]. The intensity of the bands at 1300–1400 cm^{-1} also decreases for composite samples, and a new small peak at 990 cm^{-1} is noticed (shoulder in neat chitosan FTIR spectrum), revealing strong interactions between the nanomagnetite and the amide/amino groups of the chitosan. Moreover, the spectra of the nanocomposites show a broad absorption band in the region of 700–500 cm^{-1} due to the iron oxide skeleton [24,31]. This pattern is consistent with the magnetite spectrum since the band located at 570 cm^{-1} is typical of Fe_3O_4 and could be useful to distinguish it between other Fe oxides [31].

The spectra of the plasticized samples (Fig. 3) present almost the same characteristics than these of glycerol-free samples, although the bands due to glycerol contribute to the absorption in the corresponding regions, increasing the intensity of the bands located at 3400–3300, 2933–2880, 1625, 1500–1200 and 1110–650 cm^{-1}.

XRD patterns of selected magnetic chitosan films with and without glycerol are shown in Fig. 4. The existence of iron oxide particles (Fe_3O_4) in the films is only clearly revealed by this technique in the films containing 10 wt% magnetite, in which the characteristic peaks for Fe_3O_4 at

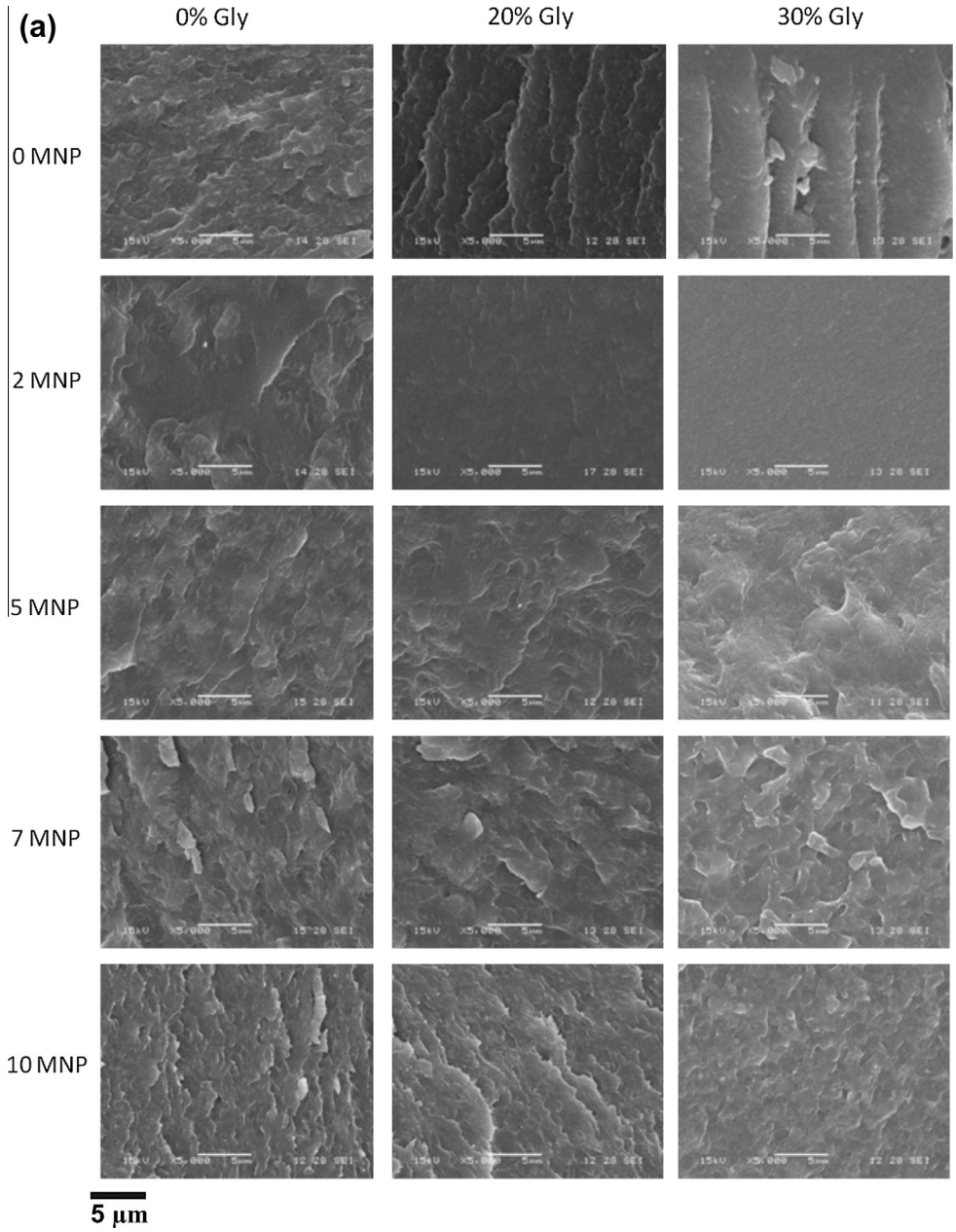

Fig. 6. SEM micrographs of the nanocomposite cross-sections (a) and surfaces (b), as a function of the magnetite concentration.

2θ = 30.1, 35.5, 43.3, 53.4, 57.2 and 62.5, 62.71, which can be indexed to (220), (311), (400), (422), (511) and (440) planes of magnetite [9,10,18], respectively, are detectable. Evidently, the strong signals of crystalline chitosan film, mainly represented by the peak centered at 20° [31], masked the magnetite contribution. However, the reflection peaks obtained in this figure are in good agreement with the standard magnetite file (JCPDS card number 19-06290), indicating that the sample has a cubic crystalline structure [9,18] and that the resultant nanoparticles were Fe_3O_4 with a spinel structure [18]. The average crystallite sizes obtained from the Scherrer equation ranged from about 5 to 13 nm for both the unplasticized and plasticized films. Similar XRD patterns were also reported for PVA-nanomagnetite films obtained by precipitating in situ the nanoparticles [32].

Although the "crystallite size" determined by DRX patterns is not necessarily synonymous of "particle size", in this case the values calculated from the Scherrer equation are similar to the particle diameters obtained from TEM images. The TEM image of the unplasticized sample with 10% MNP showed in Fig. 5 denotes that the composite film is formed by numerous magnetite nanoparticles integrated in the chitosan matrix. It is worth noting that they do not

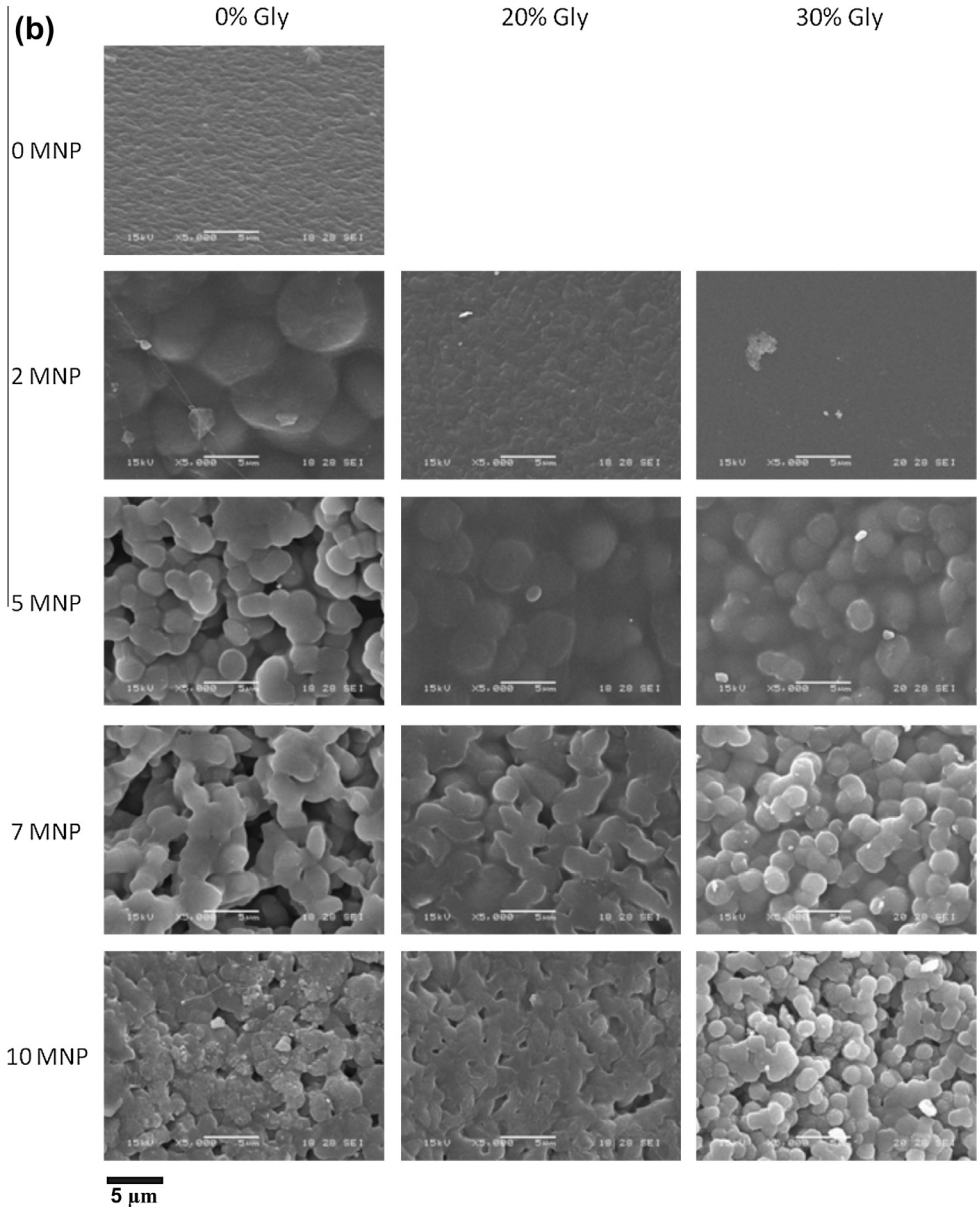

Fig. 6 (*continued*)

aggregate inside clusters to the point where they would cancel their individual magnetic moments.

Fig. 6a and b shows the morphology of the nanocomposite, cross-sections and surfaces, respectively, as a function of the magnetite concentration. It is clear that the addition of iron nanoparticles to the chitosan films causes severe changes in the film morphology. From Fig. 6a it is observed that the roughness of the cross-sections increases when the particle concentration increases, indicating increased energy dissipation during fracture [33]. The advancing crack must change path (deflection) because of the presence of the rigid filler material, in this case the magnetite nanoparticles. The higher the particle concentration, the greater the density of crack deflection sites, producing smaller and denser ripples and ridges. However, the main modification is observed by comparing plasticized or non-plasticized chitosan films without magnetite with the corresponding films containing just 2 wt% iron particles. The neat chitosan films behave in a fragile mode when frozen at liquid nitrogen temperature, even when glycerol was added and thus, they exhibit a quite rougher cross-section, which roughness decreasing as the glycerol concentration increases. Nevertheless, the fracture path becomes smoother with the addition of a low concentration of iron particles and thus fracture surface of the 2MNP containing 30 wt% glycerol is almost featureless, a characteristic expected for a monolithic homogeneous material. This behavior confirms the existence of strong

Table 2
Contact angle measurements on the films (at 3 min 45 sec).

Nominal magnetite content	Glycerol content (wt%)	Contact angle (air) (°)
0	0%	78.0 ± 2.6
2		70.8 ± 4.7
5		91.5 ± 8.0
7		91.1 ± 3.3
10		72.4 ± 3.9
0	20%	71.3 ± 3.4
2		71.5 ± 5.0
5		76.0 ± 4.1
7		79.7 ± 5.1
10		65.7 ± 4.0
0	30%	67.4 ± 4.0
2		66.6 ± 6.3
5		71.7 ± 4.6
7		75.1 ± 3.5
10		65.3 ± 6.0

interactions between the chitosan and the iron oxide. Fig. 6b serves to reinforce this assumption: the morphology of the film surfaces changes from the corresponding to a monolithic homogeneous material exhibiting a rather smooth and continuous surface (0MNP, 0% glycerol; 0 and 2MNP, 20% glycerol; 0 and 2MNP, 30% glycerol) to a globular one, with a co-continuous structure (2MNP, 0% glycerol; 5MNP, 20% glycerol; 5MNP, 30% glycerol) to finally reaching a totally globular morphology with the globules connected among them, instead having a continuous connecting matrix (ex. 5, 7 and 10MNP, 0% glycerol; 7 and 10MNP, 20% glycerol; 7 and 10MNP, 30% glycerol). The amount of globules increases as particle concentration increases, while it size decreases. For the non-plasticized or containing 20 wt% glycerol and 10% nanoparticles, the globule shape becomes somewhat irregular and these formations seems to collapse into larger domains.

Table 2 presents the results of contact angle measured on the upper film surfaces (side in contact with air during the drying step). The contact angle is one of the basic wetting properties of materials that reveal the hydrophilic/hydrophobic character of the film surface. In our case, measurements were performed using ethylene glycol, a polar solvent and thus, an increase in the contact angle indicates a density reduction of polar groups on the film surface. It can be noticed that plasticized film surfaces are more hydrophilic than non-plasticized ones and that nanocomposites containing intermediate concentrations of inorganic particles exhibit the more hydrophobic surface characters. Evidently the important changes in the microstructure of the film surfaces with increasing concentrations of nanoparticles (Fig. 6b), could also affect its wettability by the solvent. As previously stated, the film surface evolves from a continuous chitosan matrix with included nodules (neat or low particle content samples) to a quite porous structure (intermediate particle concentrations) with increasing roughness to finally reach a less porous morphology due to increased connections between globules. This last effect became quite important for the 10 wt% MNP films and thus the contact angles significantly decrease for this composition.

Fig. 7 shows the moisture absorbed by the different films as a function of the time of storage in a container maintained at 95% RH. The sorption pattern of all the samples is quasi-Fickean, presenting an overshoot at lower times that flattens for longer times, a behavior that was observed for other films based on chitosan.

Table 3 presents the equilibrium moisture content and the effective diffusion coefficient of all samples. It is noticed that both values decrease as magnetite content increases, indicating that nanocomposites are less hydrophilic than

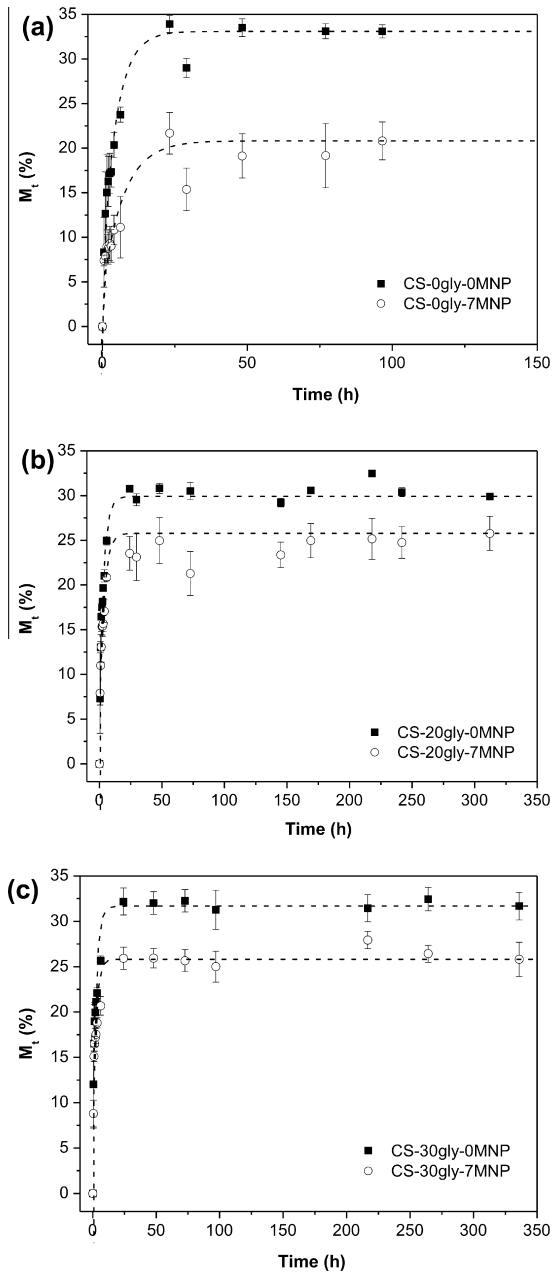

Fig. 7. Moisture absorption of films as a function of magnetite and glycerol concentration and time of storage in a 95% RH ambient. (a) 0 wt% glycerol, (b) 20 wt% glycerol and (c) 30 wt% glycerol.

Table 3
Equilibrium moisture content and effective diffusion coefficient of nanocomposite films, measured at 95% RH.

Nominal magnetite content	Glycerol content (wt%)	EMC (%)	D_{ef} (m^2/s) ($\times 10^{14}$)
0	0%	33.09 ± 0.74	33.2 ± 10.4
2		29.50 ± 1.33	8.81 ± 1.04
5		23.91 ± 1.42	10.3 ± 2.46
7		22.04 ± 2.99	8.44 ± 1.69
0	20%	29.91 ± 0.18	36.4 ± 2.80
2		29.69 ± 1.30	22.9 ± 2.92
5		26.17 ± 1.97	15.9 ± 2.87
7		25.78 ± 1.90	32.2 ± 6.49
0	30%	31.68 ± 1.53	32.1 ± 7.72
2		29.35 ± 1.35	27.0 ± 2.54
5		28.12 ± 1.83	26.8 ± 5.07
7		25.81 ± 1.88	12.6 ± 1.83

the unfilled chitosan films and that the presence of particles also complicated the path for water diffusion by increasing the tortuosity. The decrease in the affinity for water of the films with the addition of magnetite can be attributed to interactions between matrix and particles. The formations of complexes Fe—chitosan have been previously reported in the scientific literature [21,34]. It was established that in the presence of OH-moieties (last step of composite films preparation, immersion in NaOH solution) the ferric and ferrous ions chelated by the amino groups [(chitosan—NH_2)$_2$—Fe^{2+}, (chitosan—NH_2)$_2$—Fe^{3+}] provided nucleation sites for magnetite crystals growth [35]. The postulated mechanism could justify the results from FTIR. Moreover, Lassalle et al. [31] found, from Z potential measurements, that the magnetite–chitosan composite nanoparticles exhibited a positive charged surface, which indicates that electrostatic interactions between chitosan and magnetite cannot be discarded and would contribute to the iron oxide linkage on polymeric networks. On the other hand, the behavior regarding glycerol concentration it is not clear. On one side the equilibrium moisture content seems to decreases slightly with the increase of glycerol content, while the effective diffusion coefficients are almost unaffected (notice the large error bars associated to samples without magnetite).

Since glycerol is a hydrophilic plasticizer, the expected behavior was that it facilitates and increases water absorption. However, conformational changes of the polymer chains when the films were formed from solutions containing both glycerol and water can justify this behavior because some of the chitosan hydrophilic sites resulted blocked by hydrophilic groups of glycerol. In other words it seems that glycerol and chitosan interact more favorably between them than with water molecules.

Table 4 presents the results of the tensile tests performed on the films. The complete stress vs. deformation curve was only obtained from the more deformable samples (i.e. those containing low particle concentration or high amount of plasticizer), since the other samples were too fragile to cut in the dumbbell shape required by the ASTM standard. Even though, in some cases only the tensile modulus could be calculated, since specimens failed before reaching the ultimate deformation. From Table 4 it can be noticed that the average values corresponding to the tensile modulus of the composite films decreased as the magnetite concentration increases if non-plasticized chitosan is used as matrix. However, the standard deviation of these values is quite high and thus, there are not really significant differences between samples. On the other hand, the tensile modulus increases as the concentration of iron oxide particles increases if the matrix is based on chitosan plasticized with glycerol, which is the expected behavior since inorganic particles are much more stiff than the polymeric matrix. The ultimate strength does not exhibit a clear trend, neither respect to magnetite concentration, nor respect glycerol one, but the ultimate deformation clearly decreases with increasing concentrations of particles, another expected behavior since the mobility of the matrix polymer chains is restricted by the rigid particles that strongly interact with them.

Fig. 8 shows the thermo-mechanical behavior of composite films prepared with 30% glycerol. In all cases (including composites made with 0% and 20% glycerol), the storage modulus of nanomagnetite-reinforced films resulted higher than that of the corresponding matrices, in the whole range of temperatures analyzed. Moreover, as the particle concentration increases the storage modulus also increases, confirming the reinforcing effect of magnetite. Moreover, in general the storage modulus increases as the temperature increases, due to the loss of moisture of the samples that were previously conditioned at 65% RH,

Table 4
Tensile properties of nanocomposite films.

Nominal magnetite content	Glycerol content (wt%)	E (MPa)	σ_b (MPa)	ε_b (%)
0	0%	–	–	–
2		1480.4 ± 363.9	48.0 ± 3.2	10.1 ± 4.5
5		1187.9 ± 376.4	47.7 ± 4.9	9.8 ± 1.4
0	20%	1015.8 ± 243.1	35.6 ± 4.1	10.7 ± 2.7
2		1432.6 ± 162.7	44.7 ± 5.3	19.4 ± 4.1
5		1876.5 ± 436.8	41.9 ± 3.2	6.5 ± 1.3
0	30%	1155.8 ± 289.6	34.5 ± 2.7	19.0 ± 4.4
2		1389.6 ± 436.1	36.2 ± 5.4	15.6 ± 6.0
5		1318.8 ± 198.5	35.0 ± 1.7	8.7 ± 1.8
7		1920.8 ± 446.1	42.9 ± 6.4	6.9 ± 2.4

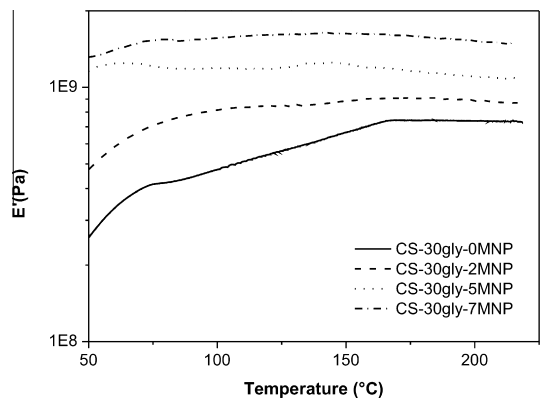

Fig. 8. Thermo-mechanical behavior of selected composite films.

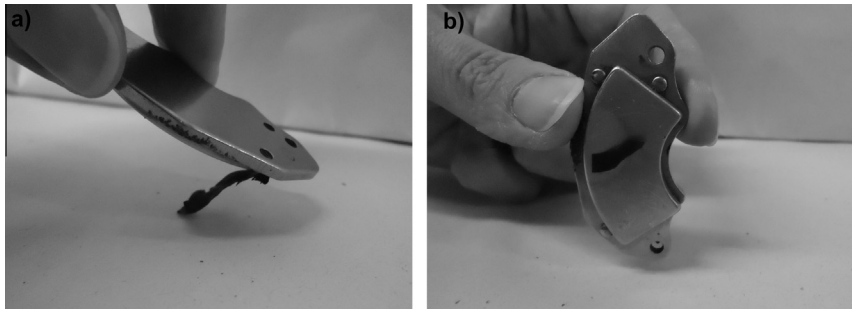

Fig. 9. Magnetic behavior of the nanocomposite film CS-0gly-10MNP.

but the differences in the values corresponding to low (i.e. 50 °C) and high (i.e. 200 °C) reduces as iron oxide concentration increases, due to the reduced hydrophilic character of composite samples. Moreover, chitosan based films exhibit strain hardening up to the point of rupture in tensile mechanical tests (Ref. [23], own results) and this behavior could contribute to increase the storage modulus as the test progress, since a tensile static stress superimposed to an oscillating one cyclic were applied.

The magnetic behavior of composite samples was qualitatively evaluated. Fig. 9a shows the behavior of the non-plasticized nanocomposite film with 10% MNP while it approaches a magnet and Fig. 9b its final situation, clearly confirming that the composite has magnetic behavior. This performance was also shown by all the non-plasticized nanocomposite films, except the one containing just 2% MNP and by reinforced samples based on chitosan plasticized with 20% glycerol, although in these last cases the magnetic character seems to be lower, as if the plasticizer interferes with the ordering of magnetic moments of the particles.

4. Conclusions

Complex chitosan-plasticized and non-plasticized films reinforced with nanomagnetite precipitated "in situ" were successfully obtained by solvent-casting. The content of iron oxide in the final films was estimated by thermogravimetry, with results differing from the nominal ones without a clear trend. Nanoparticle size estimated from DRX measurements agreed with TEM observations, indicating that individual nanoparticles, instead of clusters, were precipitated inside the polymeric matrix. Moreover, TG analysis together FTIR and moisture sorption tests indicated that different kind of strong interactions between nanomagnetite particles and chitosan matrix were developed and thus, composites are less thermal stable but also less hydrophilic than the corresponding matrices. The addition of nanomagnetite to the chitosan matrix causes important changes in both the superficial and global microstructure of the films that led to different contact angles and to a more fragile but stiff behavior as particle concentration increases. Finally, composites with magnetite content higher than 2 wt% exhibited magnetic behavior, which corroborated the well dispersion of the particles into the polymeric matrices.

Acknowledgements

The authors gratefully acknowledge the financial support provided by the National Research Council of Argentina (CONICET, Grant PIP 0637), the Science and Technology National Promotion Agency (ANPCyT, Grant PICT-2013-1535) and the National University of Mar del Plata (Project # 15/G377).

References

[1] Zhang LD, Liu WL, Xiao CL, Yao JS, Fan ZP, Sun XL, et al. Preparation of poly(styrene)-β-poly(acrylic acid)/γ-Fe_2O_3 composites. J Magn Magn Mater 2011;323:3087–91.
[2] Zhou LL, Yuan JY, Yuan WZ, Sui XF, Wu SZ, Li ZL, et al. Synthesis, characterization, and controllable drug release of pH-sensitive hybrid magnetic nanoparticles. J Magn Magn Mater 2009;321:2799–804.
[3] Sharifi I, Shokrollahi H, Amiri S. Ferrite-based magnetic nanofluids used in hyperthermia applications. J Magn Magn Mater 2012;324:903–15.
[4] Karimi Z, Karimi L, Shokrollahi H. Nano-magnetic particles used in biomedicine: core and coating materials. Mater. Sci. Eng. C 2013;33:2465–75.
[5] Fang C, Bhattarai N, Sun C, Zhang M. Functionalized nanoparticles with long-term stability in biological media. Small 2009;5(14):1637–41.
[6] Zavisova V, Koneracká M, Muckova M, Lazová J, Juríková A, Lancz G, et al. Magnetic fluid poly(ethylene glycol) with moderate anticancer activity. J Magn Magn Mater 2010;323:1408–12.
[7] Wilson JL, Poddar P, Frey NA, Srikanth H, Mohomed K, Harmon JP, et al. Synthesis and magnetic properties of polymer nanocomposites with embedded iron nanoparticles. J Appl Phys 2004;95:1439–43.
[8] Sondjaja R, Hatton TA, Tam MKC. Clustering of magnetic nanoparticles using a double hydrophilic block copolymer, poly(ethylene oxide)-b-poly(-acrylic acid). J Magn Magn Mater 2009;321:2393–7.
[9] Bhatt AS, Krishna Bhat D, Santosh MS. Electrical and magnetic properties of chitosan–magnetite nanocomposites. Physica B 2010;405:2078–82.
[10] Zhang L, Zhu X, Sun H, Chi G, Xu J, Sun Y. Control synthesis of magnetic Fe_3O_4—chitosan nanoparticles under UV irradiation in aqueous system. Curr Appl Phys 2010;10:828–33.
[11] Yuwei C, Jianlong W. Preparation and characterization of magnetic chitosan nanoparticles and its application for Cu(II) removal. Chem Eng J 2011;168:286–92.
[12] Mahmoudi M, Sant S, Wang B, Laurent S, Sen T. Superparamagnetic iron oxide nanoparticles (SPIONs): development, surface modification and applications in chemotherapy. Adv Drug Deliv Rev 2010;63:24–46.
[13] Xu C, Cai H, He P, Fang Y. Electrochemical detection of sequence-specific DNA using a DNA probe labeled with aminoferrocene and chitosan modified electrode immobilized with ssDNA. Analyst 2001;126:62–5.
[14] Neuberger T, Schopf B, Hofmann H, Hofmann M. Superparamagnetic nanoparticles for biomedical applications: possibilities and limitations of a new drug delivery system. J Magn Magn Mater 2005;293:483–96.

[15] Kaushik A, Khan R, Solanki PR, Pandey P, Alam, Ahmad JS, et al. Iron oxide nanoparticles-chitosan composite based glucose biosensor. Biosens Bioelectron 2008;24:676–83.
[16] Kaushik A, Solanki PR, Ansari AA, Sumana G, Ahmad S, Malhotra BD. Iron oxide–chitosan nanobiocomposite for urea sensor. Sens. Actuators, B 2009;138:572–80.
[17] Donia AM, Atia AA, Elwakeel KZ. Recovery of gold(III) and silver(I) on a chemically modified chitosan with magnetic properties. Hydrometallurgy 2007;87:197–206.
[18] Chen J, Yang P, Ma Y, Wu T. Characterization of chitosan magnetic nanoparticles for in situ delivery of tissue plasminogen activator. Carbohydr Polym 2011;84:364–72.
[19] Char K, Park MJ. Selective distribution of interacting magnetic nanoparticles into block copolymer domains based on the facile inversion of micelles. React Funct Polym 2009;69:546–51.
[20] Hu Q, Chen F, Li B, Shen J. Preparation of three-dimensional nano-magnetite/chitosan rod. Mater Lett 2006;60:368–70.
[21] Li B, Jia D, Zhou Y, Hu Q, Cai W. In situ hybridization to chitosan/magnetite nanocomposite induced by the magnetic field. J Magn Magn Mater 2006;306:223–7.
[22] Crank J. The mathematics of diffusion. 1st ed. Oxford: Clarendon; 1956.
[23] Pereda M, Aranguren MI, Marcovich NE. Characterization of chitosan/caseinate films. J Appl Polym Sci 2008;107(2):1080–90.
[24] Belessi V, Zboril R, Tucek J, Mashlan M, Tzitzios V, Petridis D. Ferrofluids from magnetic–chitosan hybrids. Chem Mater 2008;20:3298–305.
[25] Hritcu D, Popa MI, Popa N, Badescu V, Balan V. Preparation and characterization of magnetic chitosan nanospheres. Turk J Chem 2009;33:785–96.
[26] Benavides Rodríguez L, Sibaja Ballestero M, Vega-Baudrit J, Camacho Elizondo M, Madrigal Carballo S. Estudio cinético de la degradación térmica de quitina y quitosano de camarón de la especie "heterocarpus vicarius" empleando la técnica termogravimétrica en modo dinámico. Rev Iberoam Polím 2010;11(7):558–73.
[27] Pawlak A, Mucha M. Thermogravimetric and FTIR studies of chitosan blends. Thermochim Acta 2003;396:153–66.
[28] Udrea LE, Hritcu D, Popa MI, Rotariu O. Preparation and characterization of polyvinyl alcohol–chitosan biocompatible magnetic microparticles. J Magn Magn Mater 2011;323:7–13.
[29] Sipos P, Berkesi O, Tombácz E, Pierre TGSt, Webb J. Formation of spherical iron(III) oxyhydroxide nanoparticles sterically stabilized by chitosan in aqueous solutions. J Inorg Biochem 2003;95:55–63.
[30] El Fray M, Niemczyk A, Pabin-Szafko B. Chemical modification of chitosan with fatty acids. Prog. Chem. Appl. Chitin Derivatives 2012;XVII:29–36.
[31] Lassalle VL, Zysler RD, Ferreira ML. Novel and facile synthesis of magnetic composites by a modified co-precipitation method. Mater Chem Phys 2011;130:624–34.
[32] Sinha A, Chakraborty J, Das SK, Das S, Rao V, Ramachandrarao P. Oriented arrays of nanocrystalline magnetite in polymer matrix produced by biomimetic synthesis. Mater Trans 2001;42(8):1672–5.
[33] Marcovich NE, Bellesi NE, Auad ML, Nutt SR, Aranguren MI. Cellulose micro/nanocrystals reinforced polyurethane. J Mater Res 2006;21(4):870–81.
[34] Guibal E. Interactions of metal ions with chitosan-based sorbents: a review. Sep. Purif. Technol. 2004;38:43–74.
[35] Wang Y, Li B, Zhou Y, Jia D. In situ mineralization of magnetite nanoparticles in chitosan hydrogel. Nanoscale Res Lett 2009;4:1041–6.